Enhanced Polysulfide Conversion with Highly Conductive and Electrocatalytic Iodine-Doped Bismuth Selenide Nanosheets in Lithium-Sulfur Batteries

Mengyao Li,[†,‡,+] *Dawei Yang,*[*,‡,‡,+], *Jordi Jacas Biendicho,*[†] *Xu Han,*[§] *Chaoqi Zhang,*[†,‡] *Kun Liu,*[○] *Jiefeng Diao,*[□] *Junshan Li,*[//] *Marc Heggen,*[#] *Rafal E. Dunin-Borkowski,*[#] *Jiaao Wang,*[*,□] *Graeme Henkelman,*[□] *Joan Ramon Morante,*[†,‡] *Jordi Arbiol,*[§,⊥] *Shu-Lei Chou,*[*,&] *Andreu Cabot*[*,†,⊥]

[†] Catalonia Institute for Energy Research-IREC, Sant Adrià de Besòs, Barcelona, 08930, Spain.

[‡] Department of Electronic and Biomedical Engineering, Universitat de Barcelona, 08028, Barcelona, Spain.

[§] Catalan Institute of Nanoscience and Nanotechnology (ICN2), CSIC and BIST, Campus, UAB, Bellaterra, 08193, Barcelona, Spain.

[○] Institute of Materials and Technology, Dalian Maritime University, Dalian 116026, China.

[□] Department of Chemistry and the Oden Institute for Computational Engineering and Sciences, The University of Texas at Austin, Austin, TX, 78712 USA.

[//] Institute of Advanced Study, Chengdu University, 610106 No. 2025, Chengluo Avenue, Chengdu, Sichuan Province, China.

[#] Ernst Ruska-Centre for Microscopy and Spectroscopy with Electrons and Peter Grünberg Institute, Forschungszentrum Jülich GmbH, Jülich, 52425 Germany.

[&] Institute for Carbon Neutralization, College of Chemistry and Materials Engineering, Wenzhou University, Wenzhou, Zhejiang 325035, China.

[⊥] ICREA, Pg. Lluís Companys 23, 08010, Barcelona, Spain.

[+] These authors contributed equally to this work

Email: daweiirec@163.com

Email: wangjiaao0720@utexas.edu

Email: chou@wzu.edu.cn

Email: acabot@irec.cat

ABSTRACT

Lithium-sulfur batteries (LSBs) are a particularly promising candidate for next-generation energy storage systems owing to their high energy density and large potential for low cost and minimum environmental impact. However, their commercialization is still hindered by limitations of the sulfur cathode, mainly the lithium polysulfide (LiPS) dissolution and shuttling, and the sluggish sulfur redox kinetics. Herein, we propose an innovative sulfur host, based on an iodine-doped bismuth selenide (I-Bi_2Se_3), able to solve these limitations by immobilizing the LiPS and catalytically activating the redox conversion at the cathode. We detail here the synthesis of I-Bi_2Se_3 nanosheets and thoroughly characterize their morphology, crystal structure and composition. We use density-functional theory and experimental tools to demonstrate that I-Bi_2Se_3 nanosheets are characterized by a proper composition and micro- and nano-structure to facilitate Li^+ diffusion and fast electron transportation, and to provide numerous surface sites with strong LiPS adsorbability and extraordinary catalytic activity.

Overall, I-Bi_2Se_3/S electrodes exhibit outstanding initial capacities up to 1500 mAh g^{-1} at 0.1 C and cycling stability over 1000 cycles, with an average capacity decay rate of only 0.012% per cycle at 1 C. Besides, at a sulfur loading of 5.2 mg cm^{-2}, a high areal capacity of 5.70 mAh cm^{-2} at 0.1 C is obtained with an electrolyte/sulfur ratio of 12 µL mg^{-1}.

Keywords: Bismuth selenide, nanosheet, iodine-doped, lithium polysulfide, lithium-sulfur battery

There is an urgent need for a new generation of rechargeable energy storage devices that offer a step higher capacity and durability, well beyond the limitations of current lithium-ion batteries (LIBs). Among the possible candidates, lithium-sulfur batteries (LSBs) attract significant attention due to their very high theoretical specific energy, 2600 Wh Kg^{-1}, their potential for low cost associated with the abundance of sulfur, and their lack of toxicity.[1–5] However, their practical use is still hindered by the electrically insulating nature of sulfur and its discharge products (Li_2S/Li_2S_2),[6–8] a low utilization of the active material, and a moderate cycling stability associated with the large volume expansion of the cathode upon lithiation[9–12] and the shuttle of the soluble intermediate lithium polysulfides (LiPS).[13–15] These drawbacks call for an improved design and engineering of the sulfur cathode.[16–20]

Conductive porous carbons have been widely used to improve the electrical conductivity of the cathode, encapsulate sulfur and restrain the dissolution and diffusion of LiPS.[21,22] However, the encapsulation of sulfur within porous carbon can be detrimental to the cathode redox reaction kinetics by reducing sulfur reactivity and slowing the desolvation process.[23,24] To overcome current cathode limitations, metal-based compounds and metal-organic frameworks have been added to strengthen the chemical interaction with LiPS and reduce the shuttle effect.[25–29]

Among the tested metal compounds, sulfides such as MoS_2, VS_2, CoS_2, Ni_3S_2, and Sb_2S_3, have demonstrated particularly strong sulfiphilic ability toward LiPS trapping and low lithiation voltages.[30–35] However, cathodes based on metal sulfides are generally characterized by moderate electrical conductivities, limited sulfur utilization, insufficient cycling stability and low rate capabilities.[36–40]

Recently, we and others have demonstrated metal selenides, such as ZnSe, $NbSe_2$ and $NiCo_2Se_4$, as promising sulfur hosts in LSB cathodes, owing to their notable polarity, excellent catalytic activity, and high electrical conductivity.[3,5,33,41] However, among the extended family of possible chalcogenides, a particularly interesting candidate has been so far overlooked. Bismuth selenide (Bi_2Se_3) is generally an n-type degenerated semiconductor, with a low bandgap of 0.3 eV, that is widely used in the field of thermoelectricity due to its high electrical conductivity.[41, 42] Its n-type electronic behavior is related to the presence of Se vacancies that act as electron donors. Bi_2Se_3 has a layered crystal structure consisting of stacks of covalently bonded quintuple atomic layers, Se-Bi-Se-Bi-Se, that are held together by weak van der Waals interactions. Such high electrical conductivity and layered structure is highly suitable for its use as sulfur hosts in LSB cathodes. Besides, the variable chemical valences of Bi and Se anticipates a high potential catalytic activity.

In this work, we evaluate the potential of iodine-doped Bi_2Se_3 nanosheets as sulfur host in LSBs. We first detail the synthesis of Bi_2Se_3 nanosheets using a high yield and scalable solution-based method. These Bi_2Se_3 nanosheets are doped with iodine to further improve their adsorption and catalytic activity. The obtained material is used as sulfur host in LSB cathodes and its performance is experimentally analyzed and computationally rationalized. Results demonstrate the I-Bi_2Se_3 nanosheets to provide high electrical conductivity, enhanced confinement of LiPS,

the mitigation of the sulfur volume expansion effects, and an excellent electrocatalytic activity towards the redox reaction of sulfur and lithium sulfide.

RESULTS AND DISCUSSION

Bi_2Se_3 nanosheets, assembled into flower-like structures (Figure S1a), were produced at 180 ºC from a basic solution containing bismuth nitrate, sodium selenite and polyvinylpyrrolidone (see details in the experimental section in the supporting information). X-ray diffraction (XRD) analysis showed the nanosheets to have high crystallinity and their crystal structure to match the rhombohedral Bi_2Se_3 phase (JCPDS No. 00-033-0214, Figure S1b). High resolution transmission electron microscopy (HRTEM) characterization confirmed the Bi_2Se_3 rhombohedral phase (space group =Pbnm) with a= 11.6230 Å, b=11.8310 Å and c=4.0900 Å (Figure S1c). Besides, electron energy loss spectroscopy (EELS) chemical composition maps demonstrated a uniform distribution of both elements, Bi and Se, through the nanosheet (Figure S1d).

Iodine ions were incorporated to pre-synthesized Bi_2Se_3 by dispersing the Bi_2Se_3 nanosheets in an aqueous solution of potassium iodide under vigorous stirring at room temperature for 48 h. Iodine-doped Bi_2Se_3 (I-Bi_2Se_3) nanosheets preserved the flower-like morphology and the rhombohedral crystal structure of undoped Bi_2Se_3 (Figure 1a-c). EDX analysis quantified the iodine concentration at a 5 at%. Besides, EELS chemical composition maps displayed a homogeneous distribution of Bi, Se and I within the I-Bi_2Se_3 nanosheets (Figure 1d).

X-ray photoelectron spectroscopy (XPS) was used to determine the surface composition of I-Bi_2Se_3 and the chemical environment of its elements (Figure 1e,f,g). The high-resolution Bi 4f XPS spectrum was fitted with two doublets (Figure 1e). The lowest energy doublet was

associated with Bi^{3+} within a Bi_2Se_3 chemical environment (Bi $4f_{7/2}$ binding energy at 157.5 eV). The highest energy doublet was associated with Bi^{3+} within a more electronegative environment, as it could be Bi_2O_3, $Bi_2(SeO_3)_3$, Bi_2SeO_2 or another oxidized form of Bi_2Se_3 (Bi $4f_{7/2}$ binding energy at 158.5 eV).[44, 45] The presence of an oxide component was related to the transportation and handling of the particles in the air. The high-resolution Se 3d XPS spectrum was also fitted with two doublets (Figure 1f), which were associated with Se^{2-} within Bi_2Se_3 (Se $3d_{5/2}$ at 52.8 eV) and SeO_2, $Bi_2(SeO_3)_3$, Bi_2SeO_2 or another form of Se within a more electronegative environment (Se $3d_{5/2}$ at 53.7 eV), related to the partial oxidation of the material surface.[42,44] The high resolution I 3d XPS spectrum was fitted with two peaks, at 618.5 eV (I $3d_{5/2}$) and 630 eV ($3d_{3/2}$), which were associated with an I^{-1} chemical state (Figure 1i).[46]

The electrical conductivity of both Bi_2Se_3 and I-Bi_2Se_3 samples decreased with temperature, implying a degenerated semiconductor behavior (Figure 1f). Besides, the Seebeck coefficient of both samples was negative in the whole temperature range, implying an n-type conductivity. With the introduction of iodine, a twofold increase of the Bi_2Se_3 electrical conductivity was measured. The rise of the electrical conductivity was correlated with a decrease of the absolute value of the Seebeck coefficient, which is consistent with an increase of the charge carrier concentration with the iodine doping.

Sulfur was introduced via a melt-diffusion process (see details in the experimental section).[5,33] The morphology of the I-Bi_2Se_3/S composite resembled that of the original I-Bi_2Se_3 nanosheets assembled into flowers (Figure 1g). EDX elemental maps displayed a homogeneous distribution of the four elements, I, Bi, Se and S, within the composite (Figure 1g), with no independent sulfur particle. Upon sulfur incorporation, the nitrogen adsorption-desorption isotherms showed the Brunauer–Emmett–Teller (BET) specific surface area to be reduced from

128.6 m^2 g^{-1} for I-Bi_2Se_3 to 13.2 m^2 g^{-1} for I-Bi_2Se_3/S (Figure S3). Besides, the pore volume of I-Bi_2Se_3, decreased from 0.5 cm^3 g^{-1}, to 0.026 cm^3 g^{-1} with the incorporation of sulfur, which further demonstrated the successful loading of sulfur within the pore structure of the assembled I-Bi_2Se_3 nanosheets. The loaded mass of sulfur was quantified at *ca.* 70.2 wt% using thermogravimetry analysis (TGA, Figure S2).

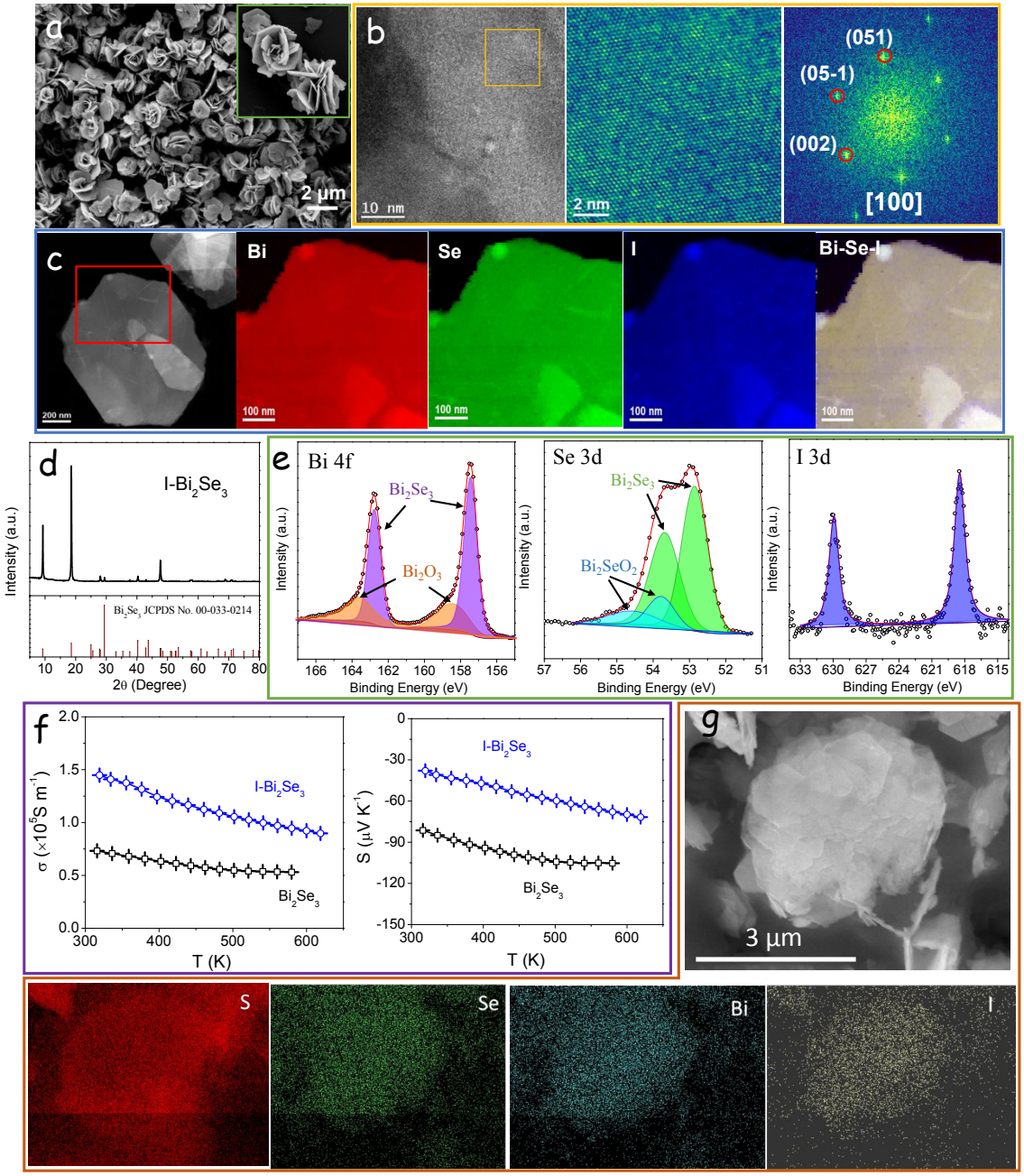

Figure 1. Characterization of I-Bi_2Se_3 nanosheets: (a) SEM image. (b) HRTEM image and its corresponding power spectrum. (c) EELS chemical composition maps obtained from the red

squared area of the STEM micrograph. Individual Bi $N_{6,7}$-edges at 157 eV (red), Se M_1-edge at 232 eV (green), I $M_{4,5}$-edge 619 eV (blue) and composite of Bi-Se-I. (d) XRD pattern. (e) Bi 4f, Se 3d and I 3d high-resolution XPS spectra. (f) Temperature dependence of the electrical conductivity (σ) and Seebeck coefficient (S) of Bi_2Se_3 and I-Bi_2Se_3. (g) SEM image EDX elemental maps of I-Bi_2Se_3/S composite.

The interaction between I-Bi_2Se_3 and LiPS was analyzed using Li_2S_4 adsorption tests (see details in experimental section). Figure 2a,b displays an optical image and the UV-vis spectra of several flasks that contain 3 mL of a 0.01 M Li_2S_4 solution and the exact same amount (20 mg) of each of the tested adsorbers, Super P, Bi_2Se_3 or I-Bi_2Se_3, after overnight ageing. We observe that the color of the Li_2S_4 solution, and the absorbance intensity in the 400–500 nm region associated with Li_2S_4, was almost unchanged in the presence of Super P. On the contrary, the color of the Li_2S_4 solutions and the visible absorbance became much lighter in the presence of Bi_2Se_3 and especially I-Bi_2Se_3, suggesting a strong chemical interaction of LIPS with Bi_2Se_3 and particularly with I-Bi_2Se_3. I-Bi_2Se_3 exhibited the clearest solution and the lowest visible absorption, indicating the presence of the lowest amount of Li_2S_4 in the solution and thus the greatest LiPS adsorbability.

Figure 2c displays the high-resolution Bi 4f XPS spectra of I-Bi_2Se_3 before and after the Li_2S_4 adsorption test. Compared with the original spectra of I-Bi_2Se_3, the Bi 4f binding energies in I-Bi_2Se_3-Li_2S_4 shifted to lower values, revealing the interaction of S with surface Bi.[5]

Density functional theory (DFT) calculations were carried out to further evaluate the interaction between LiPS and I-Bi_2Se_3. The optimized LiPS adsorption configuration at six different lithiation stages (Li_2S, Li_2S_2, Li_2S_4, Li_2S_6, Li_2S_8 and S_8) on the Bi_2Se_3 and I-Bi_2Se_3 surfaces are displayed in Figures S4 and S5. DFT calculations showed the binding energies (E_b) of LiPS species at the six tested lithiation stages to be higher on I-Bi_2Se_3 than on Bi_2Se_3 (Figure 2e).

Figure 2d displays the relaxed adsorption structure of Li_2S_4 on the (110) surface of Bi_2Se_3 and I-Bi_2Se_3, respectively. The calculated E_b for the relaxed configuration of Li_2S_4 absorbed on Bi_2Se_3 (110) and I-Bi_2Se_3 (110) surfaces are -1.27 eV and -2.09 eV, respectively. These DFT results demonstrate a strong interaction between S within LiPS and Bi within Bi_2Se_3, which corroborates the sulfiphilic character of Bi_2Se_3. These results also demonstrate that the presence of I on the Bi_2Se_3 surface further increases the absolute value of the binding energy, thus favoring LiPS adsorption and hence potentially reducing the shuttle effect.

Figure 2f displays the band structure and density of states (DOS) of Bi_2Se_3 and I-Bi_2Se_3. Calculations show I-Bi_2Se_3 to be characterized by a significantly smaller bandgap than Bi_2Se_3. Besides, consistently with results from electrical transport measurements, DFT calculations show the presence of iodine to upward shift the Fermi level, which appears lying within the I-Bi_2Se_3 conduction band thus promoting the intrinsic conductivity and degenerated/metallic character of I-Bi_2Se_3.[47]

Figure 2g and Figure S6 exhibit the initial state, transition state and final state of Li_2S decomposition on Bi_2Se_3 and I-Bi_2Se_3. The calculated energy barrier for Li_2S decomposition on Bi_2Se_3 and I-Bi_2Se_3 surfaces was 0.56 and 0.98 eV, respectively (Figure 2g). These results demonstrate that I-Bi_2Se_3 can greatly reduce the Li_2S decomposition energy barrier and enhance the redox reversibility between Li_2S and LiPS.

The S reduction pathways on both Bi_2Se_3/S and I-Bi_2Se_3/S cathodes were calculated considering the overall reversible reaction between Li_2S and S_8 + Li. The first step of the discharge process involves the reduction of S_8 with two Li^+ to form Li_2S_8. Subsequently, Li_2S_8 undergoes further reduction to three intermediate LiPS, Li_2S_6, Li_2S_4, Li_2S_2 and finally Li_2S as the end product. Figure 2h displays the optimized configuration of the intermediates and their

Gibbs free energy profiles. For both materials, Bi_2Se_3/S and I-Bi_2Se_3/S, the largest increase of Gibbs free energy was obtained for the conversion from Li_2S_2 to Li_2S, suggesting this step as the rate-limiting for the discharge process.[48] The free energy increase of this step was lower for I-Bi_2Se_3 (0.71 eV) than for Bi_2Se_3 (0.89 eV), suggesting that the reduction of S was more thermodynamically favorable on I-Bi_2Se_3 than on Bi_2Se_3.

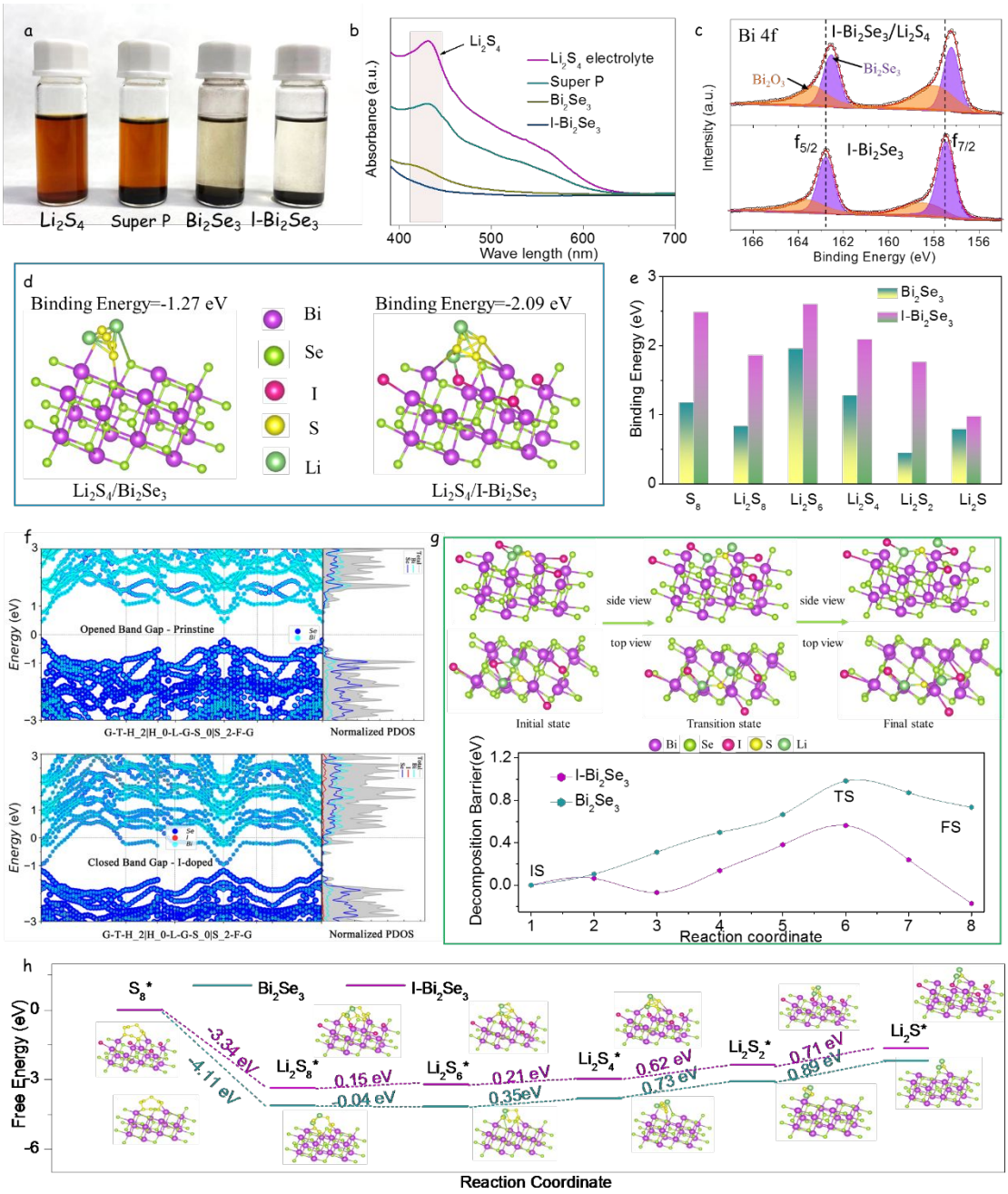

Figure 2. (a) Optical photograph of flasks containing 3 mL of a 0.01 M Li_2S_4 solution and 20 mg of Super P, Bi_2Se_3 or I-Bi_2Se_3 after overnight ageing. (b) UV–vis spectra of the supernatants.

(c) Bi 4f XPS spectra of I-Bi_2Se_3 before and after Li_2S_4 adsorption. (d) Optimized geometrical configurations of Li_2S_4 on Bi_2Se_3 and I-Bi_2Se_3 surfaces. (e) Calculated binding energies of LiPS (Li_2S, Li_2S_2, Li_2S_4, Li_2S_6, Li_2S_8 and S_8) on Bi_2Se_3 and I-Bi_2Se_3 surfaces. (f) HSE06 band structure and density of states of Bi_2Se_3 and I-Bi_2Se_3. (g) Optimized adsorption configuration for the Li_2S decomposition on I-Bi_2Se_3 and energy barrier profiles of Li_2S cluster decomposition on Bi_2Se_3 and I-Bi_2Se_3 along with different reaction coordinates. (h) Gibbs free energy profiles and optimized adsorption conformation of LiPS species on Bi_2Se_3 and I-Bi_2Se_3, showing a much lower reaction free energy from Li_2S_2 to Li_2S on I-Bi_2Se_3 than on Bi_2Se_3.

The electrochemical performance of Li-S coin cells containing an I-Bi_2Se_3/S cathode was evaluated and compared with that of cells based on Bi_2Se_3/S and Super P/S cathodes. Figure 3a displays the CV curves obtained at 0.1 mV s^{-1}. All cathodes displayed two well-defined cathodic peaks associated with the reduction of solid-state S into soluble long-chain LiPS (Li_2S_x, $4 < x < 8$, peak C1) and the subsequent conversion of these LiPS to insoluble Li_2S_2/Li_2S (peak C2).[3] Besides, an anodic peak is observed (peak A), corresponding to the reverse oxidation conversion from Li_2S to LiPS and ultimately to S.[33] The peak current density of the reduction and oxidation peaks of I-Bi_2Se_3/S was clearly higher than that of the two reference cathodes, all containing the same amount of sulfur, thus suggesting a higher sulfur utilization in the I-Bi_2Se_3/S cathode. The C2 peak of the I-Bi_2Se_3/S cathode at about 2.042 V shows a much larger current density and is slightly shifted to a higher potential compared with the other cathodes, suggesting a promoted conversion of LiPS to insoluble Li_2S_2/Li_2S within the I-Bi_2Se_3/S cathode. Besides, the A oxidation peak of I-Bi_2Se_3/S is shifted to a lower potential, 2.33 V, and displays a larger current density, indicating an enhanced Li_2S decomposition (Figure 3a,b).

The onset potentials at a current density of 10 μA cm^{-2} beyond the baseline current were used to quantitatively estimate the electrocatalytic activity (Figure 3b and S8).[23] Cells based on I-

Bi_2Se_3/S cathodes showed the highest onset potentials of cathodic peaks and the lowest onset potentials for the anodic peak, which further demonstrates the accelerated redox kinetics obtained with the I-doped Bi_2Se_3 nanosheets. Figure S7 displays the first five CV cycles measured from I-Bi_2Se_3/S cells. All CV curves almost overlapped, which suggests excellent reversibility of the sulfur redox reactions.

CV tests at different scan rates in the range 0.1-0.5 mV s^{-1} were conducted to investigate the reaction kinetics and the lithium-ion diffusion properties of I-Bi_2Se_3/S (Figure 3c). The peak current density of the I-Bi_2Se_3/S cathode increases with the scan rate, and its shape is maintained, which denotes good electrochemical stability. In contrast, Bi_2Se_3/S and especially Super P/S cathodes display more remarkable changes in the CV curve when increasing the scan rate, denoting limited reaction kinetics (Figure S9).

I-Bi_2Se_3/S cathodes exhibited a linear relationship between the cathodic and anodic peak currents and the square root of the scanning rate, as it corresponds to a diffusion-limited process (Figure 3d-f). From the fitting of this linear dependence, the diffusion constant of the rate-limiting species, *i.e.* lithium ions (D_{Li+}), was calculated according to the Randles-Sevcik equation:[5]

$$I_P = (2.69 * 10^5) n^{1.5} A D_{Li+}^{0.5} C_{Li+} v^{0.5} \quad (1)$$

where I_p is the peak current density, n is the number of charges transferred, A is the geometric area of the electrode, C_{Li+} is the concentration of lithium ions in the cathode, and v is the scan rate. I-Bi_2Se_3/S electrodes displayed the sharpest I_P *vs* $v^{0.5}$ slopes, indicating the fastest lithium-ion diffusion in both the reduction and oxidation processes. According to the Randles-Sevcik equation, the values of D_{Li+} calculated for I-Bi_2Se_3/S at peaks C1, C2 and A were 2.3 ×

10^{-7}, 3.7×10^{-7}, and 5.9×10^{-7} cm^2 s^{-1}, respectively. All these values were well above those obtained for Bi_2Se_3/S and Super P/S electrodes (Figure 3g). Taking into account the similar morphology of I-Bi_2Se_3 and Bi_2Se_3, the enhanced lithium-ion diffusivities must be related to the improved catalytic activity of the former, which accelerates the LiPS conversion, and to the stronger LiPS adsorption that suppresses the shuttle effect and prevents the deposition of an insulating layer at the anode side.[49]

To further analyse the electrocatalytic activity of the different materials toward the polysulfide conversion, CV profiles were measured on symmetric cells within the voltage window -1.0 to 1.0 V and using a 0.5 M Li_2S_6 electrolyte (Figure 3h).[5,33] To eliminate the capacitive contribution, the CV curve of I-Bi_2Se_3 in a Li_2S_6-free electrolyte was also measured as a reference (Figure S10). The CV curve of the symmetric cells with a Li_2S_6-free electrolyte delivered a low current, well below that of CV curves of all symmetric cells having Li_2S_6 in their electrolyte, which indicates that the lithiation/delithiation reactions dominate the current response.[50] Besides, the I-Bi_2Se_3 symmetric cells including Li_2S_6 additive exhibited a much higher current density than those of Bi_2Se_3 and Super P cells, which we associate with an enhanced polysulfide absorption and a higher catalytic activity.

The Li_2S nucleation and dissolution processes were analysed to investigate the liquid-solid reaction kinetics. Compared with the Bi_2Se_3 cathode, the I-Bi_2Se_3 cathode exhibited significantly shorter nucleation and growth times and a higher discharging peak current during the potentiostatic measurement at 2.05 V (Figure 3i). Based on Faraday´s law, the capacity of the I-Bi_2Se_3 electrode was calculated at 287.5 mAh g^{-1}, well above that of the Bi_2Se_3 electrode, 206.8 mAh g^{-1}.[51] Taking into account the similar morphology and crystal structure of the two

materials, the significant differences obtained must be ascribed to the effect of iodine doping, which significantly improves the Li_2S precipitation kinetics.

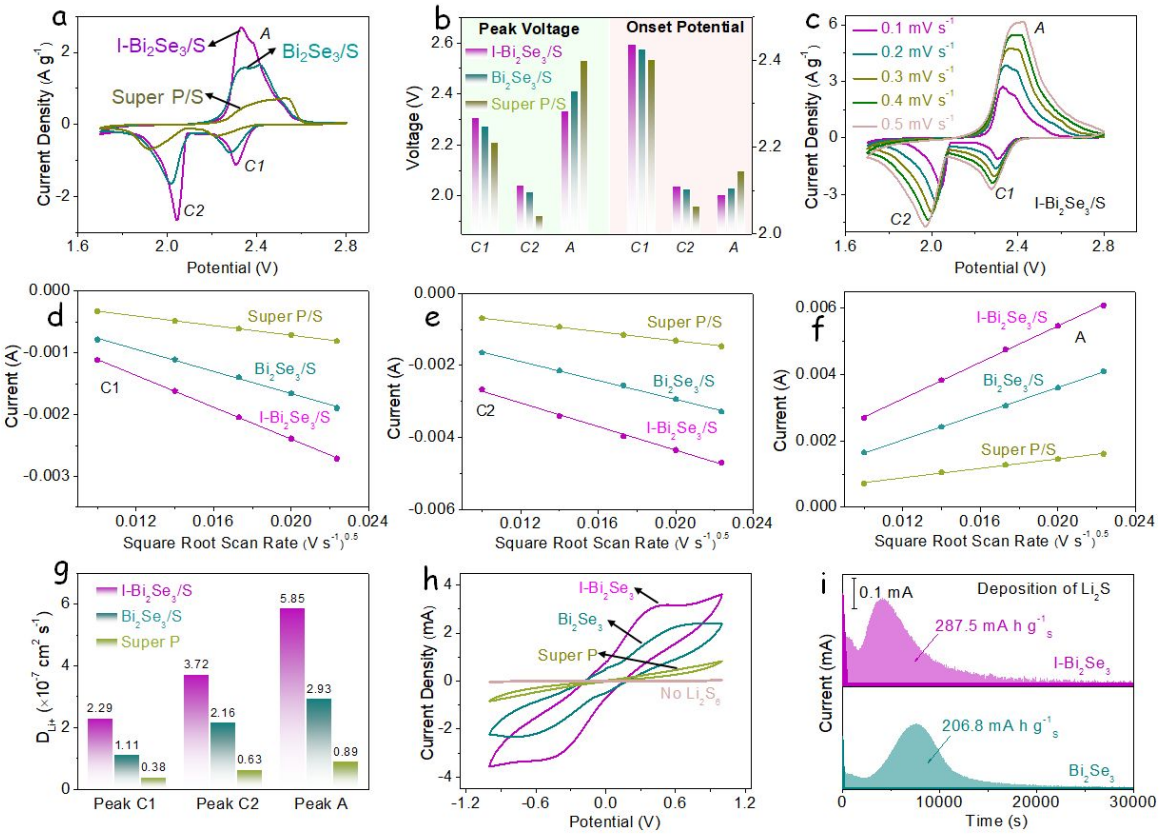

Figure 3. (a) CV profiles of Li–S cells with I-Bi_2Se_3/S, Bi_2Se_3/S and Super/S cathodes at a 0.1 mV s^{-1} scan rate. (b) Peak potential and onset potential of asymmetrical Li–S cells obtained from CV curves. (c) CV profiles of the I-Bi_2Se_3/S electrode at scan rates from 0.1 to 0.5 mV s^{-1}. (d) Peak current vs the square root of the scan rate (υ) for the cathodic reduction processes (C1, C2) and anodic oxidation process (A) in Li–S cells with different electrodes. (e) Li^+ diffusion coefficient calculated from the CV redox peaks according to the Randles−Sevcik equation. (f) CV curves of symmetric cells at a scan rate of 20 mV s^{-1}. (g) Potentiostatic discharge profile at 2.05 V on different electrodes with Li_2S_8 catholyte for evaluating the nucleation kinetics of Li_2S.

The galvanostatic charge/discharge curves of I-Bi_2Se_3/S, Bi_2Se_3/S and Super P/S electrodes at a current density of 0.1 C (1672 mA g^{-1}) are shown in Figure 4a. Charge/discharge curves display two discharge plateaus and one charge plateau, consistently with CV curves. The first

discharge plateau at around 2.3 V is related to the reduction of sulfur to soluble LiPS ($S_8 \rightarrow S_6^{2-} \rightarrow S_4^{2-}$).[52] The second discharge plateau corresponds to the conversion of soluble LiPS to lithium sulfide ($S_4 \rightarrow Li_2S_2 \rightarrow Li_2S$) at about 2.1 V.[53] The voltage difference between the oxidation and the second reduction plateaus is considered as the polarization potential, ΔE.[54] Among the tested materials, I-Bi_2Se_3/S showed the lowest ΔE, at 131 mV, well below that of Bi_2Se_3/S, 162 mV, and Super P/S, 205 mV (Figure 4b).

Q1 and Q2 are defined as the capacity of the first and the second discharge plateaus, respectively. Q1 measures the amount of soluble polysulfides created and potentially diffusing to the Li metal anode. Q2 measures how efficiently the created polysulfides are reduced to Li_2S. Thus the ratio Q2/Q1 can be used as a measure of the catalytic activity for LiPS conversion reaction.[55] The Q2/Q1 ratio for I-Bi_2Se_3/S was 2.71, close to the theoretical limit of 3, and well above the values obtained from Bi_2Se_3/S and Super P/S, 2.23 and 1.85, respectively (Figure 4b). The high Q2/Q1 ratio of I-Bi_2Se_3/S implies a high catalytic activity toward polysulfide's redox reaction.

The charge and discharge profiles of the different electrodes displayed in Figure S11show the I-Bi_2Se_3/S electrode to be characterized by significantly lower overpotentials for phase conversion between soluble LiPS and insoluble Li_2S_2/Li_2S, which further demonstrates the enhanced electrochemical kinetics of I-Bi_2Se_3/S.[56]

The galvanostatic charge/discharge voltage profiles of I-Bi_2Se_3/S electrodes at various current densities, from 1.0 C to 4 C, are shown in Figure 4c. Two discharge plateaus and one charge plateau were maintained even at the highest current rates tested, which is in contrast with the results obtained from Super P/S electrodes (Figure S12). An outstanding initial specific capacity of 1496 mAh g^{-1} was measured from the I-Bi_2Se_3/S electrode. Additionally, this electrode demonstrated a superior rate performance, with average discharge capacities of 1361, 1168,

1002, 897, 795 and 651 mAh g^{-1} at current rates from 0.1 C to 4 C, respectively (Figure 4d). Even when the current density was returned to 0.2 C, the specific capacity of the I-Bi_2Se_3/S electrode was recovered to 1138 mAh g^{-1}, suggesting high stability even after the high rate charge/discharge process. All these values were clearly above those obtained from Bi_2Se_3/S and Super P/S electrodes.

Among the tested materials, the cells based on I-Bi_2Se_3/S were also characterized by the highest energy efficiencies (Figure 4e), as calculated from $E = \int UIdt$.[57] I-Bi_2Se_3/S based cells displayed an energy efficiency of 89.7% at 4 C, higher than Bi_2Se_3/S (85.7%) and Super P/S (66.1%) cells. The high energy efficiency measured for I-Bi_2Se_3/S was consistent with the lower polarization potential and higher catalytic properties of I-Bi_2Se_3.

Figure 4f shows the cycling performance of the different cathodes. In this test, the first three cycles were measured at a current density of 0.1C, and then 100 cycles were tested at a current density of 0.2C. The three electrodes showed a notably stable cycling performance during 100 cycles, with a coulombic efficiency (CE) above 99%. At 0.2C, I-Bi_2Se_3/S electrodes displayed a high initial specific capacity (1274 mAh g^{-1}), well above that of Bi_2Se_3/S (1045 mAh g^{-1}), and Super P/S (727 mAh g^{-1}). After 100 cycles, 97.7% of the initial capacity was still retained for the I-Bi_2Se_3/S electrodes (1245 mAh g^{-1}). In contrast, the Bi_2Se_3/S cathode maintained just an 84.4% (882 mAh g^{-1}) of the initial discharge capacity, and the Super P/S cathode preserved just a 69.6% (506 mAh g^{-1}) of the initial capacity. The capacity loss in these cathodes was mainly associated with the dissolution of polysulfides into the electrolyte. Thus the high cycling stability of I-Bi_2Se_3/S was related to the effective inhibition of this dissolution.

Electrochemical impedance spectroscopy (EIS) was used to gain understanding of the parameters behind the enhanced redox kinetics of I-Bi_2Se_3/S electrodes. Figure 4g and S13

display the Nyquist plots of the EIS data obtained from I-Bi_2Se_3/S, Bi_2Se_3/S and Super P/S coin cells before and after cycling. The fresh electrodes displayed a semicircle in the high-frequency region associated with the charge-transfer resistance (R_{ct}), followed by a linear dependence in the low-frequency region that is related to the diffusion of lithium ions.[58] After charge/discharge loops, an additional semicircle appeared in the high-frequency range, which is associated with the deposition of the insulating discharge products of Li_2S on the electrode surface (R_{in}) during cycling. Based on the equivalent circuit displayed in Figure S13,[59] the I-Bi_2Se_3/S electrode has a considerably lower R_{in} and R_{ct} compared with Bi_2Se_3/S and Super P/S electrodes. These lower resistances indicate that the I-Bi_2Se_3/S electrode is characterized by a faster polysulfide conversion reaction, as well as a faster charge transfer kinetics during lithiation/delithiation reaction.

Even at a high current rate of 1C, I-Bi_2Se_3/S electrodes displayed a high specific capacity and stable cycling performance, with an average 0.012% capacity decay per cycle after 1000 cycles and CEs above 99.6%. The performance of I-Bi_2Se_3/S electrodes in this direction was also clearly above that of Bi_2Se_3/S and Super P/S (Figure 4h).

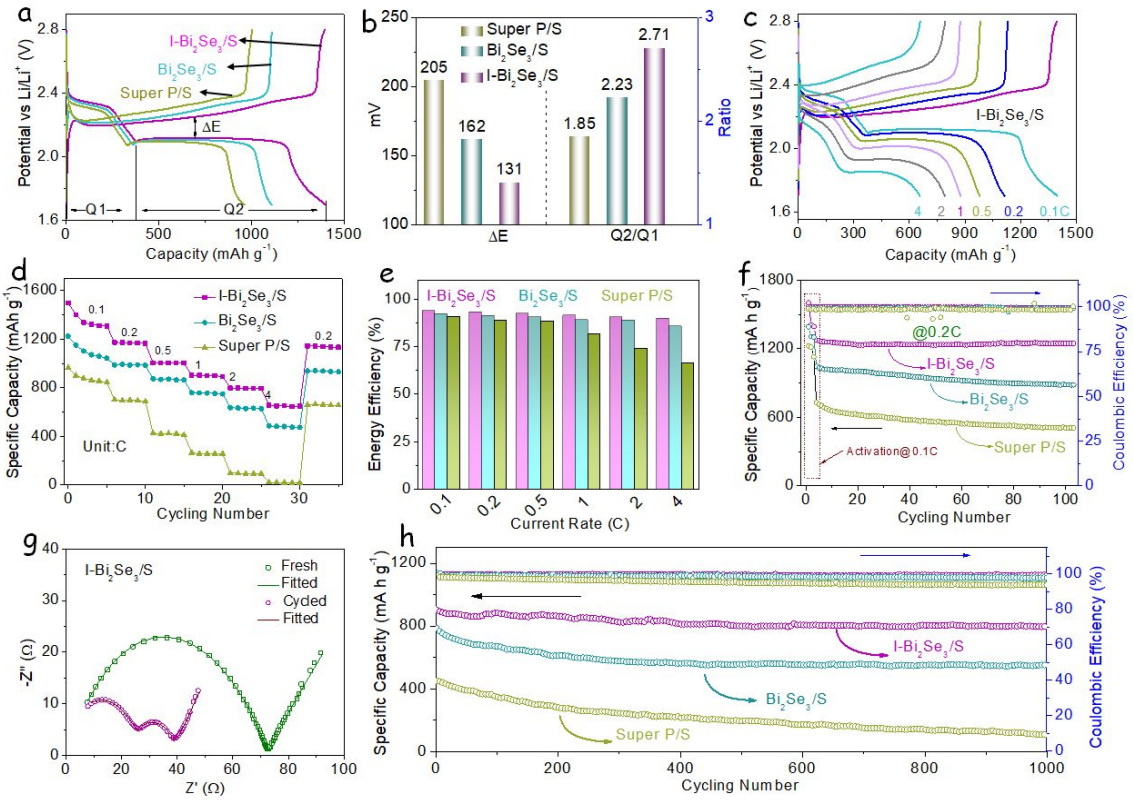

Figure 4. (a) Galvanostatic charge/discharge profiles of I-Bi_2Se_3/S, Bi_2Se_3/S and Super/S electrodes at a 0.1 C current rate. (b) ΔE and Q2/Q1 obtained from the charge/discharge curves. (c) Galvanostatic charge/discharge profiles at various rates, from 0.1 C to 4 C. (d) Rate capability of different electrodes at various C rates, from 0.1 C to 4 C. (e) Energy efficiency of different cathodes at different current rates. (f) Cycling performances of I-Bi_2Se_3/S, Bi_2Se_3/S, and Super/S electrodes at 0.2 C. (g) EIS spectrum of the I-Bi_2Se_3/S electrode after and before cycling. (h) Cycling performance and coulombic efficiency of the three cathodes at a current rate of 1 C.

I-Bi_2Se_3 electrodes were further tested with a high sulfur loading (5.2 mg cm^{-2}) and a lean electrolyte (8 μL mg^{-1}) to demonstrate their potential application in practical LSBs. As shown in Figure 5a, high sulfur loading cells exhibited an excellent rate performance, with areal capacities of 5.70 mAh cm^{-2} at 0.1C, and 4.12 mAh cm^{-2} at 0.5C, *i.e.* exceeding the industrially requested areal capacity of LIBs (~4 mAh cm^{-2}).[60] The corresponding charge/discharge profiles at different current rates are shown in Figure 5b. With the current rate increasing to 0.5C, the

discharge profile still presented the intact second plateau, demonstrating excellent electrochemical kinetics within the cell. The performance of the cell under lean electrolyte conditions, with an electrolyte/sulfur ratio of 8 μL mg^{-1}, is displayed in Figure 5c. At a current rate of 0.5C, the initial discharge capacity was 527 mAh g^{-1} and it rapidly increased to 686 mAh g^{-1} after 15 cycles. After 300 cycles, a capacity of 576 mAh g^{-1} was still measured, which corresponds to an ultralow capacity decay of 0.053% per cycle with respect to the maximum achieved capacity. Besides, I-Bi_2Se_3-based cells maintained the voltage profile during the 300 cycles, with just a small potential hysteresis, indicating a minor LiPS shuttling and stable sulfur electrochemistry (Figure S14).

Figure 5d and Table S1 display a comparison of several parameters of state-of-the-art Bi-based and Se-based materials as cathode hosts for LSBs. Notice that the I-Bi_2Se_3 host presented here is characterized by the highest capacities and stabilities. This strategy offers a new route to design multifunctional sulfur immobilizer with highly adoptive and catalytic capabilities for rapid LiPS adsorption-conversion process, holding a great promise in promoting the practical application of LSBs.

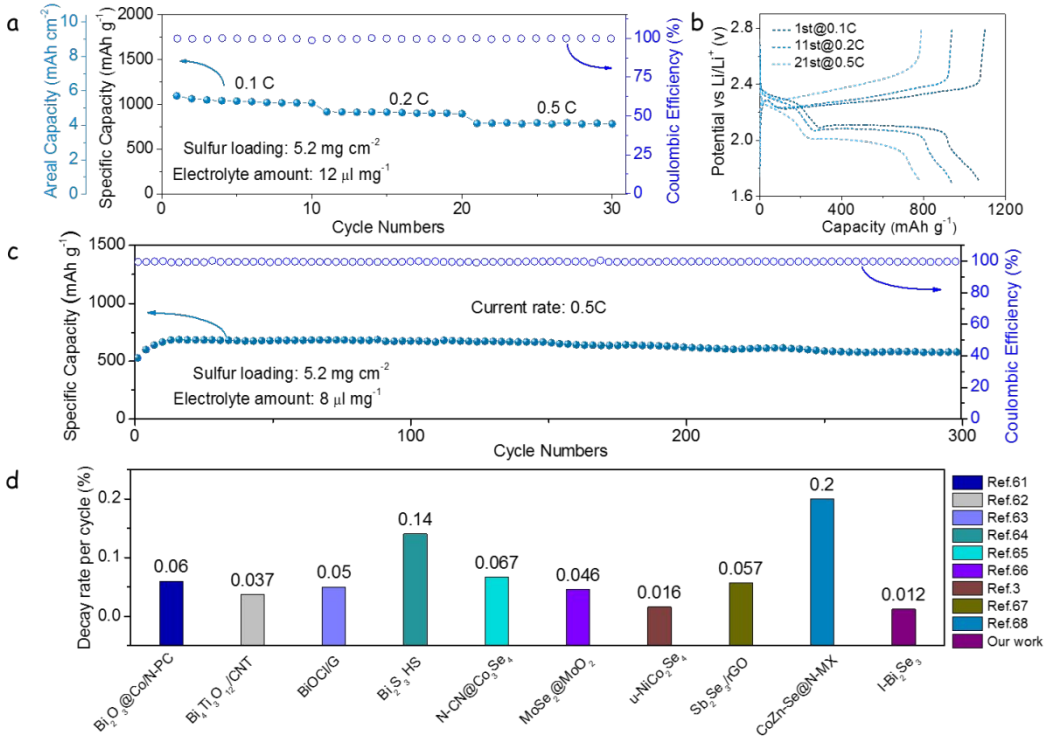

Figure 5. (a) Rate performance of the Li–S coin cells at different current rates with a sulfur loading of 5.2 mg cm^{-2}. (b) Initial charge/discharge profiles at the various current rates. (c) Cycling performances of I-Bi_2Se_3/S cathodes at a current rate of 0.5C under lean electrolyte conditions. (d) Decay rate per cycle compared with other reported works.

CONCLUSIONS

In summary, we rationally designed and engineered new LSBs cathodes based on I-Bi_2Se_3 sulfur hosts through a facile and efficient strategy. This unique architecture not only establishes a conductive framework for electron/ion transfer and buffers the volume variation of the sulfur cathode during cycling, but also constructs a multifunctional LiPS barrier that effectively suppresses polysulfide shuttling. I-Bi_2Se_3 was characterized by a high electrical conductivity due to the doping of iodine and significantly enhanced the redox kinetics of sulfur species, especially for the conversion between soluble LiPS species and Li_2S_2/Li_2S during charge/discharge processes. As a result of these excellent qualities, I-Bi_2Se_3/S cathodes deliver

excellent long-term cycling stability with a capacity decay of 0.012% per cycle over 1000 cycles at 1C. Moreover, at a sulfur loading of 5.2 mg cm^{-2}, I-Bi_2Se_3/S cathodes delivered a high areal capacity of 5.70 mAh cm^{-2}. Overall, this work shows an effective way to enhance the performance of LSB cathodes by the heteroatom doping of a metal selenide catalyst.

Supporting Information

The supporting information is available free of charge via the Internet at http://pubs.acs.org.

The supporting information includes experimental details, Figure S1-S14 and Table S1 as described in the text, specifically, additional SEM, TEM, XRD, TGA, BET, CV, electrochemical performance, DFT simulation results, and crystal structure.

Corresponding Author

Email: daweiirec@163.com

Email: wangjiaao0720@utexas.edu

Email: chou@wzu.edu.cn

Email: acabot@irec.cat

ACKNOWLEDGMENTS

The authors thank support from the projects ENE2016-77798-C4-3-R and NANOGEN (PID2020-116093RB-C43), funded by MCIN/ AEI/10.13039/501100011033/ and by "ERDF A way of making Europe", by the "European Union". M. Li, D. Yang, X. Han and C. Zhang thank the China Scholarship Council for the scholarship support. ICN2 acknowledges the support from the Severo Ochoa Programme (MINECO, grant no. SEV-2017-0706). IREC and ICN2 are both funded by the CERCA Program/Generalitat de Catalunya. This project has

received funding from the European Union's Horizon 2020 research and innovation program under grant agreement No 823717–ESTEEM3. Calculations at UT Austin were supported by the Welch Foundation (F-1841) and the Texas Advanced Computing Center. Part of the present work has been performed in the framework of Universitat Autònoma de Barcelona Materials Science PhD program.

REFERENCES

(1) Zheng, J.; Tian, J.; Wu, D.; Gu, M.; Xu, W.; Wang, C.; Gao, F.; Engelhard, M. H.; Zhang, J. G.; Liu, J.; Xiao, J. Lewis Acid-Base Interactions between Polysulfides and Metal Organic Framework in Lithium Sulfur Batteries. *Nano Lett.* **2014**, *14* (5), 2345–2352.

(2) Wang, Z.; Wang, B.; Yang, Y.; Cui, Y.; Wang, Z.; Chen, B.; Qian, G. Mixed-Metal-Organic Framework with Effective Lewis Acidic Sites for Sulfur Confinement in High-Performance Lithium-Sulfur Batteries. *ACS Appl. Mater. Interfaces* **2015**, *7* (37), 20999–21004.

(3) Zhang, C.; Biendicho, J. J.; Zhang, T.; Du, R.; Li, J.; Yang, X.; Arbiol, J.; Zhou, Y.; Morante, J. R.; Cabot, A. Combined High Catalytic Activity and Efficient Polar Tubular Nanostructure in Urchin-Like Metallic $NiCo_2Se_4$ for High-Performance Lithium–Sulfur Batteries. *Adv. Funct. Mater.* **2019**, *29* (34), 1903842.

(4) Song, Y.; Peng, Y.; Zhao, M.; Lu, Y.; Liu, J.; Li, B.; Zhang, Q. Understanding the Impedance Response of Lithium Polysulfide Symmetric Cells. *Small Sci.* **2021**, *1* (11), 2100042.

(5) Yang, D.; Liang, Z.; Zhang, C.; Biendicho, J. J.; Botifoll, M.; Spadaro, M. C.; Chen, Q.; Li, M.; Ramon, A.; Moghaddam, A. O.; Llorca, J.; Wang, J.; Morante, J. R.; Arbiol, J.; Chou, S. L.; Cabot, A. $NbSe_2$ Meets C_2N: A 2D-2D Heterostructure Catalysts as Multifunctional Polysulfide Mediator in Ultra-Long-Life Lithium–Sulfur Batteries. *Adv. Energy Mater.* **2021**, *11* (36), 2101250.

(6) Bai, S.; Liu, X.; Zhu, K.; Wu, S.; Zhou, H. Metal-Organic Framework-Based Separator for Lithium-Sulfur Batteries. *Nat. Energy* **2016**, *1*, 16049.

(7) Zhao, C.; Dai, X.; Yao, T.; Chen, W.; Wang, X.; Wang, J.; Yang, J.; Wei, S.; Wu, Y.; Li, Y. Ionic Exchange of Metal-Organic Frameworks to Access Single Nickel Sites for Efficient Electroreduction of CO_2. *J. Am. Chem. Soc.* **2017**, *139* (24), 8078–8081.

(8) Zheng, C.; Niu, S.; Lv, W.; Zhou, G.; Li, J.; Fan, S.; Deng, Y.; Pan, Z.; Li, B.; Kang, F.; Yang, Q. H. Propelling Polysulfides Transformation for High-Rate and Long-Life Lithium–Sulfur Batteries. *Nano Energy* **2017**, *33*, 306–312.

(9) Tu, S.; Chen, X.; Zhao, X.; Cheng, M.; Xiong, P.; He, Y.; Zhang, Q.; Xu, Y. A Polysulfide-Immobilizing Polymer Retards the Shuttling of Polysulfide Intermediates in Lithium–Sulfur Batteries. *Adv. Mater.* **2018**, *30* (45), 1804581.

(10) Jiang, H.; Liu, X.-C.; Wu, Y.; Shu, Y.; Gong, X.; Ke, F.-S.; Deng, H. Metal-Organic Frameworks for High Charge-Discharge Rates in Lithium-Sulfur Batteries. *Angew. Chemie* **2018**, *130* (15), 3980–3985.

(11) Tian, M.; Pei, F.; Yao, M.; Fu, Z.; Lin, L.; Wu, G.; Xu, G.; Kitagawa, H.; Fang, X. Ultrathin MOF Nanosheet Assembled Highly Oriented Microporous Membrane as an Interlayer for Lithium-Sulfur Batteries. *Energy Storage Mater.* **2019**, *21*, 14–21.

(12) Hong, X. J.; Song, C. L.; Yang, Y.; Tan, H. C.; Li, G. H.; Cai, Y. P.; Wang, H. Cerium Based Metal-Organic Frameworks as an Efficient Separator Coating Catalyzing the Conversion of Polysulfides for High Performance Lithium-Sulfur Batteries. *ACS Nano* **2019**, *13* (2), 1923–1931.

(13) Chen, Y.; Zhang, W.; Zhou, D.; Tian, H.; Su, D.; Wang, C.; Stockdale, D.; Kang, F.; Li, B.; Wang, G. Co-Fe Mixed Metal Phosphide Nanocubes with Highly Interconnected-Pore Architecture as an Efficient Polysulfide Mediator for Lithium-Sulfur Batteries. *ACS Nano* **2019**, *13* (4), 4731–4741.

(14) Shen, J.; Xu, X.; Liu, J.; Liu, Z.; Li, F.; Hu, R.; Liu, J.; Hou, X.; Feng, Y.; Yu, Y.; Zhu, M. Mechanistic Understanding of Metal Phosphide Host for Sulfur Cathode in High-Energy-Density Lithium-Sulfur Batteries. *ACS Nano* **2019**, *13* (8), 8986–8996.

(15) Jin, B.; Yang, L.; Zhang, J.; Cai, Y.; Zhu, J.; Lu, J.; Hou, Y.; He, Q.; Xing, H.; Zhan, X.; Chen, F.; Zhang, Q. Bioinspired Binders Actively Controlling Ion Migration and Accommodating Volume Change in High Sulfur Loading Lithium–Sulfur Batteries. *Adv. Energy Mater.* **2019**, *9* (48), 1902938.

(16) Li, Z.; Xiao, Z.; Wang, S.; Cheng, Z.; Li, P.; Wang, R. Engineered Interfusion of Hollow Nitrogen-Doped Carbon Nanospheres for Improving Electrochemical Behavior and Energy Density of Lithium–Sulfur Batteries. *Adv. Funct. Mater.* **2019**, *29* (31), 1902322.

(17) Xie, J.; Li, B. Q.; Peng, H. J.; Song, Y. W.; Zhao, M.; Chen, X.; Zhang, Q.; Huang, J. Q. Implanting Atomic Cobalt within Mesoporous Carbon toward Highly Stable Lithium–Sulfur Batteries. *Adv. Mater.* **2019**, *31* (43), 1903813.

(18) Zhang, L.; Liu, D.; Muhammad, Z.; Wan, F.; Xie, W.; Wang, Y.; Song, L.; Niu, Z.; Chen, J. Single Nickel Atoms on Nitrogen-Doped Graphene Enabling Enhanced Kinetics of Lithium–Sulfur Batteries. *Adv. Mater.* **2019**, *31* (40), 1903955.

(19) Chen, H.; Xiao, Y.; Chen, C.; Yang, J.; Gao, C.; Chen, Y.; Wu, J.; Shen, Y.; Zhang, W.; Li, S.; Huo, F.; Zheng, B. Conductive MOF-Modified Separator for Mitigating the Shuttle Effect of Lithium-Sulfur Battery through a Filtration Method. *ACS Appl. Mater. Interfaces* **2019**, *11* (12), 11459–11465.

(20) He, Y.; Qiao, Y.; Chang, Z.; Cao, X.; Jia, M.; He, P.; Zhou, H. Developing A "Polysulfide-Phobic" Strategy to Restrain Shuttle Effect in Lithium–Sulfur Batteries. *Angew. Chemie* **2019**, *131* (34), 11900–11904.

(21) Li, B.; Kong, L.; Zhao, C.; Jin, Q.; Chen, X.; Peng, H.; Qin, J.; Chen, J.; Yuan, H.; Zhang, Q.; Huang, J. Expediting Redox Kinetics of Sulfur Species by Atomic-scale Electrocatalysts in Lithium–Sulfur Batteries. *InfoMat* **2019**, *1* (4), 533–541.

(22) Zheng, Y.; Zheng, S.; Xue, H.; Pang, H. Metal-Organic Frameworks for Lithium-Sulfur Batteries. *J. Mater. Chem. A* **2019**, *7* (8), 3469–3491.

(23) Chu, H.; Noh, H.; Kim, Y. J.; Yuk, S.; Lee, J. H.; Lee, J.; Kwack, H.; Kim, Y. K.; Yang, D. K.; Kim, H. T. Achieving Three-Dimensional Lithium Sulfide Growth in Lithium-Sulfur Batteries Using High-Donor-Number Anions. *Nat. Commun.* **2019**, *10*, 188.

(24) Zhou, S.; Yang, S.; Yang, S.; Ding, X.; Lai, Y.; Nie, H.; Zhang, Y.; Chan, D.; Duan, H.; Huang, S.; Yang, Z. Dual-Regulation Strategy to Improve Anchoring and Conversion of Polysulfides in Lithium-Sulfur Batteries. *ACS Nano* **2020**, *14* (6), 7538–7551.

(25) Luo, L.; Li, J.; Yaghoobnejad Asl, H.; Manthiram, A. In-Situ Assembled VS_4 as a Polysulfide Mediator for High-Loading Lithium-Sulfur Batteries. *ACS Energy Lett.* **2020**, *5* (4), 1177–1185.

(26) Sun, Z.; Vijay, S.; Heenen, H. H.; Eng, A. Y. S.; Tu, W.; Zhao, Y.; Koh, S. W.; Gao, P.; Seh, Z. W.; Chan, K.; Li, H. Catalytic Polysulfide Conversion and Physiochemical Confinement for Lithium–Sulfur Batteries. *Adv. Energy Mater.* **2020**, *10* (22), 201904010.

(27) Cheng, Z.; Wang, Y.; Zhang, W.; Xu, M. Boosting Polysulfide Conversion in Lithium-Sulfur Batteries by Cobalt-Doped Vanadium Nitride Microflowers. *ACS Appl. Energy Mater.* **2020**, *3* (5), 4523–4530.

(28) Li, G.; Lu, F.; Dou, X.; Wang, X.; Luo, D.; Sun, H.; Yu, A.; Chen, Z. Polysulfide Regulation by the Zwitterionic Barrier toward Durable Lithium-Sulfur Batteries. *J. Am. Chem. Soc.* **2020**, *142* (7), 3583–3592.

(29) Liu, W.; Luo, C.; Zhang, S.; Zhang, B.; Ma, J.; Wang, X.; Liu, W.; Li, Z.; Yang, Q. H.; Lv, W. Cobalt-Doping of Molybdenum Disulfide for Enhanced Catalytic Polysulfide Conversion in Lithium-Sulfur Batteries. *ACS Nano* **2021**, *15* (4), 7491–7499.

(30) Feng, T.; Zhao, T.; Zhu, S.; Zhang, N.; Wei, Z.; Wang, K.; Li, L.; Wu, F.; Chen, R. Anion-Doped Cobalt Selenide with Porous Architecture for High-Rate and Flexible Lithium–Sulfur Batteries. *Small Methods* **2021**, *5* (9), 1–10.

(31) Ma, Z.; Liu, Y.; Gautam, J.; Liu, W.; Chishti, A. N.; Gu, J.; Yang, G.; Wu, Z.; Xie, J.; Chen, M.; Ni, L.; Diao, G. Embedding Cobalt Atom Clusters in CNT-Wired MoS_2 Tube-in-Tube Nanostructures with Enhanced Sulfur Immobilization and Catalyzation for Li–S Batteries. *Small* **2021**, *17* (39), 2102710.

(32) Zhou, X.; Meng, R.; Zhong, N.; Yin, S.; Ma, G.; Liang, X. Size-Dependent Cobalt Catalyst for Lithium Sulfur Batteries: From Single Atoms to Nanoclusters and Nanoparticles. *Small Methods* **2021**, *5* (10), 2100571.

(33) Yang, D.; Zhang, C.; Biendicho, J. J.; Han, X.; Liang, Z.; Du, R.; Li, M.; Li, J.; Arbiol, J.; Llorca, J.; Zhou, Y.; Morante, J. R.; Cabot, A. ZnSe/N-Doped Carbon Nanoreactor with Multiple Adsorption Sites for Stable Lithium-Sulfur Batteries. *ACS Nano* **2020**, *14* (11), 15492–15504.

(34) Zhang, Y.; Yang, S.; Zhou, S.; Zhang, L.; Gu, B.; Dong, Y.; Kong, S.; Cai, D.; Fang, G.; Nie, H.; Yang, Z. Oxygen Doping in Antimony Sulfide Nanosheets to Facilitate Catalytic Conversion of Polysulfides for Lithium-Sulfur Batteries. *Chem. Commun.* **2021**, *57* (26), 3255–3258.

(35) Zhang, Y.; Liu, J.; Wang, J.; Zhao, Y.; Luo, D.; Yu, A.; Wang, X.; Chen, Z. Engineering Oversaturated Fe-N_5 Multi-functional Catalytic Sites for Durable Lithium-Sulfur Batteries. *Angew. Chemie* **2021**, 202108882.

(36) Li, Y.; Lin, S.; Wang, D.; Gao, T.; Song, J.; Zhou, P.; Xu, Z.; Yang, Z.; Xiao, N.; Guo, S. Single Atom Array Mimic on Ultrathin MOF Nanosheets Boosts the Safety and Life of Lithium–Sulfur Batteries. *Adv. Mater.* **2020**, *32* (8), 1906722.

(37) Li, S.; Lin, J.; Ding, Y.; Xu, P.; Guo, X.; Xiong, W.; Wu, D.-Y.; Dong, Q.; Chen, J.; Zhang, L. Defects Engineering of Lightweight Metal–Organic Frameworks-Based Electrocatalytic Membrane for High-Loading Lithium–Sulfur Batteries. *ACS Nano* **2021**, *15* (8), 13803–13813.

(38) Zhang, T.; Hu, F.; Shao, W.; Liu, S.; Peng, H.; Song, Z.; Song, C.; Li, N.; Jian, X. Sulfur-Rich Polymers Based Cathode with Epoxy/Ally Dual-Sulfur-Fixing Mechanism for High Stability Lithium–Sulfur Battery. *ACS Nano* **2021**, *15* (9), 15027–15038.

(39) Lin, H.; Shi, H.; Wang, Z.; Mu, Y.; Li, S.; Zhao, J.; Guo, J.; Yang, B.; Wu, Z.; Liu, F. Scalable Production of Freestanding Few-Layer B12 -Borophene Single Crystalline Sheets as Efficient Electrocatalysts for Lithium-Sulfur Batteries. *ACS Nano* **2021**.

(40) Yang, T.; Xia, J.; Piao, Z.; Yang, L.; Zhang, S.; Xing, Y.; Zhou, G. Graphene-Based Materials for Flexible Lithium-Sulfur Batteries. *ACS Nano* **2021**, *15* (9), 13901–13923.

(41) Zhang, C.; Du, R.; Biendicho, J. J.; Yi, M.; Xiao, K.; Yang, D.; Zhang, T.; Wang, X.; Arbiol, J.; Llorca, J.; Zhou, Y.; Morante, J. R.; Cabot, A. Tubular CoFeP@CN as a Mott–Schottky Catalyst with Multiple Adsorption Sites for Robust Lithium−Sulfur Batteries. *Adv. Energy Mater.* **2021**, *11* (24), 1–14.

(42) Li, M.; Zhang, Y.; Zhang, T.; Zuo, Y.; Xiao, K.; Arbiol, J.; Llorca, J.; Liu, Y.; Cabot, A. Enhanced Thermoelectric Performance of N-Type Bi_2Se_3 Nanosheets through Sn Doping. *Nanomaterials* **2021**, *11* (7), 1827.

(43) Hong, M.; Chen, Z. G.; Yang, L.; Han, G.; Zou, J. Enhanced Thermoelectric Performance of Ultrathin Bi_2Se_3 Nanosheets through Thickness Control. *Adv. Electron. Mater.* **2015**, *1* (6), 1–9.

(44) Le, P. H.; Wu, K. H.; Luo, C. W.; Leu, J. Growth and Characterization of Topological Insulator Bi_2Se_3 Thin Films on $SrTiO_3$ Using Pulsed Laser Deposition. *Thin Solid Films* **2013**, *534*, 659–665.

(45) Green, A. J.; Dey, S.; An, Y. Q.; O'Brien, B.; O'Mullane, S.; Thiel, B.; Diebold, A. C. Surface Oxidation of the Topological Insulator Bi_2Se_3. *J. Vac. Sci. Technol. A Vacuum, Surfaces, Film.* **2016**, *34* (6), 061403.

(46) Li, T.; Hu, Y.; Morrison, C. A.; Wu, W.; Han, H.; Robertson, N. Lead-Free Pseudo-Three-Dimensional Organic-Inorganic Iodobismuthates for Photovoltaic Applications. *Sustain. Energy Fuels* **2017**, *1*, 308–316.

(47) Betancourt, J.; Li, S.; Dang, X.; Burton, J. D.; Tsymbal, E. Y.; Velev, J. P. Complex Band Structure of Topological Insulator Bi_2Se_3. *J. Phys. Condens. Matter* **2016**, *28*, 395501.

(48) Li, Z.; Li, P.; Meng, X.; Lin, Z.; Wang, R. The Interfacial Electronic Engineering in Binary Sulfiphilic Cobalt Boride Heterostructure Nanosheets for Upgrading Energy Density and Longevity of Lithium-Sulfur Batteries. *Adv. Mater.* **2021**, *33* (42), 2102338.

(49) Kim, S.; Lim, W.-G.; Im, H.; Ban, M.; Han, J. W.; Lee, J.; Hwang, J.; Lee, J. Polymer Interface-Dependent Morphological Transition toward Two-Dimensional Porous Inorganic Nanocoins as an Ultrathin Multifunctional Layer for Stable Lithium–Sulfur Batteries. *J. Am. Chem. Soc.* **2021**, *143* (38), 15644–15652.

(50) Zhang, H.; Ono, L. K.; Tong, G.; Liu, Y.; Qi, Y. Long-Life Lithium-Sulfur Batteries with High Areal Capacity Based on Coaxial CNTs@TiN-TiO_2 Sponge. *Nat. Commun.* **2021**, *12*, 4738.

(51) Xiao, W.; Weng, W.; Xiao, J.; Shen, Y.; Liang, X.; Lv, T. Molten Salt Electrochemical Modulation of Iron-Carbon-Nitrogen for Lithium-Sulfur Batteries. *Angew. Chemie* **2021**, *60* (47), 202111707.

(52) Kim, J.; Shin, H.; Yoo, D. J.; Kang, S.; Chung, S. Y.; Char, K.; Choi, J. W. Cobalt(II)-Centered Fluorinated Phthalocyanine-Sulfur SNAr Chemistry for Robust Lithium–Sulfur Batteries with Superior Conversion Kinetics. *Adv. Funct. Mater.* **2021**, 2106679.

(53) Liu, J.; Li, H.; Wang, J.; Zhang, Y.; Luo, D.; Zhao, Y.; Li, Y.; Yu, A.; Wang, X.; Chen, Z. Design Zwitterionic Amorphous Conjugated Micro-/Mesoporous Polymer Assembled Nanotentacle as Highly Efficient Sulfur Electrocatalyst for Lithium-Sulfur Batteries. *Adv. Energy Mater.* **2021**, *11* (40), 2101926.

(54) Ji, Y.; Yang, K.; Liu, M.; Chen, S.; Liu, X.; Yang, B.; Wang, Z.; Huang, W.; Song, Z.; Xue, S.; Fu, Y.; Yang, L.; Miller, T. S.; Pan, F. PIM-1 as a Multifunctional Framework to Enable High-Performance Solid-State Lithium–Sulfur Batteries. *Adv. Funct. Mater.* **2021**, *31* (47), 2104830.

(55) Cai, D.; Yang, J.; Liu, T.; Zhao, S.; Cao, G. Interfaces-Dominated Li_2S Nucleation Behavior Enabled by Heterostructure Catalyst for Fast Kinetics Li-S Batteries. *Nano Energy* **2021**, *89*, 106452.

(56) Huang, Y.; Shaibani, M.; Gamot, T. D.; Wang, M.; Jovanović, P.; Dilusha Cooray, M. C.; Mirshekarloo, M. S.; Mulder, R. J.; Medhekar, N. V.; Hill, M. R.; Majumder, M. A Saccharide-Based Binder for Efficient Polysulfide Regulations in Li-S Batteries. *Nat. Commun.* **2021**, *12*, 5375.

(57) Chen, S.; Song, Z.; Ji, Y.; Yang, K.; Fang, J.; Wang, L.; Wang, Z.; Zhao, Y.; Zhao, Y.; Yang, L.; Pan, F. Suppressing Polysulfide Shuttling in Lithium–Sulfur Batteries via a Multifunctional Conductive Binder. *Small Methods* **2021**, *5* (10), 2100839.

(58) Kang, H.; Park, M. J. Thirty-Minute Synthesis of Hierarchically Ordered Sulfur Particles Enables High-Energy, Flexible Lithium-Sulfur Batteries. *Nano Energy* **2021**, *89*, 106459.

(59) Wang, D.; Ma, K.; Hao, J.; Zhang, W.; Wang, C.; Xu, C.; Shi, H.; Ji, Z.; Yan, X.; Gu, Y. Multifunction Co-Nx Species to Manipulate Polysulfides Conversion Kinetics toward Highly Efficient Lithium-Sulfur Batteries. *Nano Energy* **2021**, *89*, 106426.

(60) Shang, C.; Li, G.; Wei, B.; Wang, J.; Gao, R.; Tian, Y.; Chen, Q.; Zhang, Y.; Shui, L.; Zhou, G.; Hu, Y.; Chen, Z.; Wang, X. Dissolving Vanadium into Titanium Nitride Lattice Framework for Rational Polysulfide Regulation in Li–S Batteries. *Adv. Energy Mater.* **2021**, *11* (3), 2003020.

(61) Liu, H.; Chen, Z.; Zhou, L.; Li, X.; Pei, K.; Zhang, J.; Song, Y.; Fang, F.; Che, R.; Sun, D. Rooting Bismuth Oxide Nanosheets into Porous Carbon Nanoboxes as a Sulfur Immobilizer for Lithium-Sulfur Batteries. *J. Mater. Chem. A* **2019**, *7*, 7074–7081.

(62) Zhou, Y.; Shu, H.; Zhou, Y.; Sun, T.; Han, M.; Chen, Y.; Chen, M.; Chen, Z.; Yang, X.; Wang, X. Flower-like $Bi_4Ti_3O_{12}$/Carbon Nanotubes as Reservoir and Promoter of Polysulfide for Lithium Sulfur Battery. *J. Power Sources* **2020**, *453*, 227896.

(63) Wu, X.; Liu, N.; Wang, M.; Qiu, Y.; Guan, B.; Tian, D.; Guo, Z.; Fan, L.; Zhang, N. A Class of Catalysts of BiOX (X = Cl, Br, I) for Anchoring Polysulfides and Accelerating Redox Reaction in Lithium Sulfur Batteries. *ACS Nano* **2019**, *13* (11), 13109–13115.

(64) Long, B.; Qiao, Z.; Zhang, J.; Zhang, S.; Balogun, M. S.; Lu, J.; Song, S.; Tong, Y. Polypyrrole-Encapsulated Amorphous Bi_2S_3 Hollow Sphere for Long Life Sodium Ion Batteries and Lithium-Sulfur Batteries. *J. Mater. Chem. A* **2019**, *7* (18), 11370–11378.

(65) Cai, D.; Liu, B.; Zhu, D.; Chen, D.; Lu, M.; Cao, J.; Wang, Y.; Huang, W.; Shao, Y.; Tu, H.; Han, W. Ultrafine Co_3Se_4 Nanoparticles in Nitrogen-Doped 3D Carbon Matrix for High-Stable and Long-Cycle-Life Lithium Sulfur Batteries. *Adv. Energy Mater.* **2020**, *10* (19), 1904273.

(66) Hao, Q.; Cui, G.; Zhang, Y.; Li, J.; Zhang, Z. Novel $MoSe_2$/MoO_2 Heterostructure as an Effective Sulfur Host for High-Performance Lithium/Sulfur Batteries. *Chem. Eng. J.* **2020**, *381*, 122672.

(67) Tian, Y.; Li, G.; Zhang, Y.; Luo, D.; Wang, X.; Zhao, Y.; Liu, H.; Ji, P.; Du, X.; Li, J.; Chen, Z. Low-Bandgap Se-Deficient Antimony Selenide as a Multifunctional

Polysulfide Barrier toward High-Performance Lithium–Sulfur Batteries. *Adv. Mater.* **2020**, *32* (4), 1904876.

(68) Ye, Z.; Jiang, Y.; Li, L.; Wu, F.; Chen, R. Self-Assembly of 0D–2D Heterostructure Electrocatalyst from MOF and MXene for Boosted Lithium Polysulfide Conversion Reaction. *Adv. Mater.* **2021**, *33*, 2101204.

Abstract Graphics